Fifth International Symposium on Marine Propulsors
smp'17, Espoo, Finland, June 2017

Large Eddy Simulation of Propeller in Forward Mode of Operation *

Jacob Keller[1], Praveen Kumar[1], Krishnan Mahesh[1]

[1]Department of Aerospace Engineering & Mechanics, University of Minnesota, Minneapolis, USA

ABSTRACT

Large-eddy simulation (LES) is used to study the wake dynamics and far-field sound of a five-bladed marine propeller at design operating condition. Simulations of the propeller wake performed by Kumar and Mahesh (2017) are extended in the present work to study the wake dynamics and flow-generated sound. Velocity spectra at various probe points in the rotating reference frame are computed, to analyze the wake dynamics. The phase-averaged radial velocity spectra show a dominant peak at the shaft frequency at all probe locations. It is also observed that compared to the near wake, the spectra in the far wake collapse better and the energy is more distributed across various frequencies.

Propeller blades are a dominant source of unwanted noise in marine vehicles. Accurate prediction of noise generated by the propeller relies on the accuracy of the unsteady flow field obtained from the numerical simulations. Hence, the flow field obtained from LES is used to predict the far field noise at design operating condition via the Curle acoustic analogy, modified for low Mach number flows. The accuracy of the estimation of the far field noise is assessed with respect to the underlying assumptions of inter-blade interference and compactness.

Keywords LES, forward operating condition, propeller wake, acoustics, rotor noise generation.

1 INTRODUCTION

Rotors, such as propellers, helicopters and wind turbines, form an integral part of many modern engineering devices. The wake generated by these rotor systems contains complex vortical structures, which evolve from near field to far field in a complex physical fashion. It is important to understand the physics of rotor wakes in order to predict the performance of rotor systems which improves design and optimization for their use in engineering applications. The wake of a typical N-bladed rotor consists of a system of N helical tip vortices, one generated by each blade, with a single hub vortex or N root vortices. The tip vortices are connected to the hub vortex by a thin vortex sheet which is shed by the blade trailing edge as a result of varying spanwise circulation. The strength of these vortices depends on the operating condition of the rotor and the blade design.

Rotor wakes have been extensively studied in the literature since the early work of Joukowski (1912), who was the first to propose a wake model for a two-bladed propeller. Subsequently, the stability and evolution of rotor wakes have been the subject of many theoretical (Levy and Forsdyke, 1928; Widnall, 1972; Gupta and Loewy, 1974; Okulov, 2004; Okulov and Sørensen, 2007) and experimental (Stella et al., 1998, 2000; Di Felice et al., 2004; Lee et al., 2004; Felli et al., 2006, 2008, 2011; Nemes et al., 2015; Quaranta et al., 2015) studies. In addition, in the recent past, numerous computational studies have been conducted on rotor wakes using a variety of methods ranging from the traditional potential methods (Kerwin, 1986) to Reynolds-averaged Navier–Stokes (RANS) simulation (Baek et al., 2015), detached-eddy simulation (DES) (Di Mascio et al., 2014), and large eddy simulation (LES) (Di Felice et al., 2009; Chase and Carrica, 2013; Balaras et al., 2015).

Propellers are significant contributors to the overall noise generated by marine vehicles. Understanding the noise generation of rotors is critical to the reduction of unwanted sound, specifically low frequency sound that can persist for very large distances in marine settings. The physical phenomena that produce sound are highly complex, unsteady, and are not well understood. The Ffowcs-Williams and Hawkings (FW-H) acoustic analogy (1969) is the most general form of Lighthill's analogy (1952) and has three sources: the thickness (monopole), loading (dipole), and quadrupole terms. When the acoustic surface coincides with a stationary physical surface, the FW-H equation reduces to the Curle equation which eliminates the thickness source and simplifies the forms of the loading and quadrupole sources. For low Mach number, non-cavitating flows, dipole contributions are known to be the dominant source of sound. Thus, for non-cavitating marine propellers, predicting the unsteady loading of the blades is the most important factor in sound prediction. The complex, unsteady nature of this problem lends itself to LES for high fidelity prediction of the flow field and blade loading.

Recently, Kumar and Mahesh (2017) studied a propeller wake using LES and analyzed the evolution from the near to far field. The propeller that was used in their simulations was the DTMB 4381, which is a five-bladed marine propeller with no skew or rake. Their simulations used the numerical algorithm developed by Mahesh et al. (2004), which is a non-dissipative and robust finite volume method for LES on unstructured grids. This algorithm has been extensively used in the past to study crashback flows with the same propeller (Vyšohlid and Mahesh, 2006; Chang et al., 2008; Jang and Mahesh, 2008, 2012, 2013; Verma et al.,

*Email for correspondence: kmahesh@umn.edu

2012; Kumar and Mahesh, 2015) and attached flows at high Reynolds number (Chang et al., 2011; Kumar and Mahesh, 2016). Kumar and Mahesh (2017) show good agreement with experiments; they reported a mechanism of mutual-induction instability mode in which the tip vortices interact with the small trailing edge vortices, generated by the spiral roll-up of the blade trailing edge wake in the near field. They also found that the temporal spectra of thrust and torque coefficients on the propeller were broadband.

The present paper extends the analysis of Kumar and Mahesh (2017). In the present work, we perform wall-resolved LES of flow over a marine propeller (DTMB 4381) at the design advance ratio. The objectives of the present paper are to: (i) investigate the wake dynamics and (ii) use the simulated flow field to predict the rotor noise. The paper is organized as follows. The simulation details, including the numerical method, computational domain, and boundary conditions, are described in §2. The results are discussed in §3. Finally, the essential flow physics are summarized in §4.

2 SIMULATION DETAILS

2.1 Numerical method

In LES, large scales are resolved by the spatially filtered Navier–Stokes equations, whereas the effect of small scales is modelled. These LES were performed in a frame of reference that rotates with the propeller. The spatially filtered incompressible Navier–Stokes equations, in the rotating frame of reference, are formulated for the absolute velocity vector in the inertial frame as follows:

$$\frac{\partial \overline{u}_i}{\partial t} + \frac{\partial}{\partial x_j}(\overline{u}_i\overline{u}_j - \overline{u}_i\epsilon_{jkl}\omega_k x_l) = -\frac{\partial \overline{p}}{\partial x_i} - \epsilon_{ijk}\omega_j\overline{u}_k + \nu\frac{\partial^2\overline{u}_i}{\partial x_j\partial x_j} - \frac{\partial \tau_{ij}}{\partial x_j}$$
$$\frac{\partial \overline{u}_i}{\partial x_i} = 0 \qquad (1)$$

where u_i is the inertial velocity in the inertial frame, p is the pressure, x_i are coordinates in the rotating non-inertial reference frame, ω_j is the angular velocity of the rotating frame of reference, ν is the kinematic viscosity, ϵ_{ijk} denotes the permutation tensor and the approximation $\overline{u_i\epsilon_{jkl}\omega_k x_l} \approx \overline{u}_i\epsilon_{jkl}\omega_k x_l$ is used. The terms containing ω_j in Eq. (1) take into account the effect of the rotating reference frame which is non-inertial. $\frac{\partial}{\partial x_j}(-\overline{u}_i\epsilon_{jkl}\omega_k x_l)$ represents the Coriolis acceleration, whereas $-\epsilon_{ijk}\omega_j\overline{u}_k$ is representative of the centrifugal acceleration. The overbar $\overline{(\cdot)}$ denotes the spatial filter and $\tau_{ij} = \overline{u_iu_j} - \overline{u}_i\overline{u}_j$ is the sub-grid stress. The sub-grid stress is modelled by the Dynamic Smagorinsky Model (Germano et al., 1991; Lilly, 1992). The Lagrangian time scale is dynamically computed based on surrogate–correlation of the Germano–identity error (Park and Mahesh, 2009). This approach is extended to unstructured grids and has shown good performance for a variety of cases including flow past a marine propeller in crashback (Verma and Mahesh, 2012).

The algorithm is derived to be robust without any numerical dissipation. It is a finite volume method where the Cartesian velocities and pressure are stored at the centroids of the cells and the face normal velocities are stored independently at the centroids of the faces. A predictor–corrector approach is used. The predicted velocities at the control volume centroids are first obtained and then interpolated to obtain the face normal velocities. The predicted face normal velocity is projected so that the continuity equation in Eq. (1) is discretely satisfied. This yields a Poisson equation for pressure which is solved iteratively using a multigrid approach. The pressure field is used to update the Cartesian control volume velocities using a least-square formulation. Time advancement is performed using an implicit Crank–Nicholson scheme. The algorithm has been validated for a variety of problems over a range of Reynolds numbers (see Mahesh et al., 2004).

2.2 Computational domain and boundary conditions

The propeller geometry, computational domain, and the boundary conditions used in the present work are identical to that of Kumar and Mahesh (2017). The geometric details of the propeller are reported in Bridges (2004). The computational domain used in the simulations is a cylinder of diameter $7.0D$ and length $10.0D$ where, D is the diameter of the propeller disk.

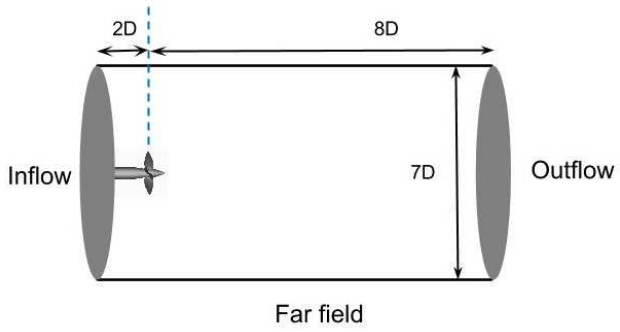

Figure 1: Computational domain and boundary conditions on the domain boundaries. (Figure is reproduced with permission from Kumar and Mahesh (2017)).

The reference coordinate system is chosen such that the blades of the propeller are located at the origin and the flow is in the positive x direction. The domain extends $2D$ upstream and $8D$ downstream of the propeller. Free-stream velocity boundary conditions are specified at the inlet and the lateral far field boundaries. Convective boundary conditions are prescribed at the outflow. Since the velocities in the governing equations (Eq. 1) are written in the inertial frame, boundary conditions on solid walls are also prescribed in the inertial frame. Thus, on the rotor, the conditions on the blades and hub are specified as $u = \omega \times r$, while those on the shaft are prescribed as no-slip boundary conditions. The computational grid used in the simulations is identical to Kumar and Mahesh (2017). It has 181 million control volumes consisting of only hexahedral cells. The grid is designed carefully to capture all the essential features of the flow field and is clustered close to all solid surfaces; ten layers of hexahedral cells are extruded from the surface with a minimum wall-normal spac-

ing of $0.0017D$ on blades and $0.00017D$ on both the hub and shaft surfaces to resolve near-wall flow features. A growth ratio of 1.02 is applied at all solid surfaces to transition from fine to coarser resolution away from the surface. The grid is refined in the wake region of the propeller to capture the small scales. A schematic of the computational domain and the boundary conditions are shown in Figure 1. The entire grid is partitioned over 2048 processors and the simulations are performed with a time step $\Delta tU/D = 8.33 \times 10^{-5}$, where U is the free stream velocity and D is the propeller diameter; this corresponds to $10,668$ computational time steps per rotation.

2.3 Acoustics

The Ffowcs-Williams and Hawkings equation (1969) can be written in integral form using the free-space Green's function, which is valid for an acoustically compact integration surface. That is, the acoustic wavelength of the radiated sound, which depends on the speed of sound (c) and frequency (f) as $\lambda = c/f$, is larger than the characteristic size of the integration surface. If it is also assumed that the integration surface coincides with a stationary ($v_i = 0$) physical ($u_i = 0$) surface, the FW-H equation takes the form of the Curle equation that is the main result of Curle (1955),

$$\begin{aligned} 4\pi p'(\vec{x},t) = &\frac{\partial}{\partial t}\int_S \frac{\left[\rho_0 \cancel{v_n}^{0} + \rho(\cancel{u_n}^{0} - \cancel{v_n}^{0}\right]}{|1-\cancel{M_r}||\vec{r}|} dS(\vec{y},\tau) \\ &- \frac{\partial}{\partial x_i}\int_S \frac{\left[\cancel{\rho v_i}^{0}(\cancel{u_n}^{0} - \cancel{v_n}^{0}) + f_i\right]}{|1-\cancel{M_r}||\vec{r}|} dS(\vec{y},\tau) \\ &+ \frac{\partial^2}{\partial x_i x_j}\int_V \frac{T_{ij}(\vec{y},\tau)}{|1-\cancel{M_r}||\vec{r}|} dV(\vec{y},\tau) \end{aligned} \tag{2}$$

which leads to

$$\begin{aligned} 4\pi p'(\vec{x},t) = &-\frac{\partial}{\partial x_i}\int_S \frac{f_i}{|\vec{r}|} dS(\vec{y},\tau) \\ &+ \frac{\partial^2}{\partial x_i x_j}\int_V \frac{T_{ij}(\vec{y},\tau)}{|\vec{r}|} dV(\vec{y},\tau) \end{aligned} \tag{3}$$

where $\vec{x}$ and t are the observer space-time variables, $\vec{y}$ and τ are the source space-time variables, and the radiation vector is denoted as $\vec{r} = \vec{x} - \vec{y}$. The local force on the surface is expressed in terms of the compressive stress tensor, $f_i = \Delta P_{ij} n_j$, and T_{ij} is Lighthill's stress tensor. The Doppler factor $|1 - M_r|$ accounts for convective amplification, where $M_r = \hat{r}_i M_i$ is the Mach number at the surface in the direction of the radiation vector $\vec{r}$; for the stationary surface in the Curle analogy, $M_r = 0$. Also, it can be shown that $\frac{\partial^2 T_{ij}}{\partial x_i x_j} \to 0$ for low Mach number flows.

If the acoustic surface is compact, $F_i = \int_{S(\vec{y})} f_i dS(\vec{y})$ is the net force over the compact surface. F_i can be modeled as being applied at some point $\vec{y}_0$ contained by the surface $S(\vec{y})$, thus F_i is only a function of τ. Compactness also implies that $r = |\vec{x} - \vec{y}| \approx |\vec{x} - \vec{y_0}|$ and

$$p'(\vec{x},t) = -\frac{1}{4\pi}\frac{\partial}{\partial x_i}\left(\frac{F_i}{|\vec{r}|}\right) \tag{4}$$

To explore the effects of rotation y_0 can be allowed to be a function of τ, thus $r = r(\tau)$, without loss of generality. For a general source $Q_i(\tau)$ partial derivatives can be applied to find that

$$\frac{\partial Q_i}{\partial x_i} = \frac{\hat{r}_i}{c}\frac{\partial Q_i}{\partial t}\left(1 - \frac{\hat{r}_j}{c}\frac{\partial y_{0j}}{\partial \tau}\right) \tag{5}$$

In the case of a propeller rotating about the 1-axis,

$$\frac{\partial y_{0i}}{\partial \tau} = \begin{cases} 0 & \text{if } i = 1, \\ -\omega y_0 sin(\omega\tau) & \text{if } i = 2, \\ \omega y_0 cos(\omega\tau) & \text{if } i = 3. \end{cases}$$

For the computation of sound in the far-field,

$$\begin{aligned} \frac{\partial Q_i}{\partial t} &= \frac{1}{|\vec{r}|}\frac{\partial F_i}{\partial t} - \frac{F_i}{|\vec{r}|^2}\frac{\partial |\vec{r}|}{\partial t} \\ &\approx \frac{1}{|\vec{r}|}\frac{\partial F_i}{\partial t} \end{aligned} \tag{6}$$

where $Q_i = F_i/|\vec{r}|$. Thus, the Curle analogy becomes

$$p'(\vec{x},t) \approx \frac{1}{4\pi}\frac{\hat{r}_i}{|\vec{r}|c}\frac{\partial F_i}{\partial t}\left[1 + \frac{\omega y_0}{c}\left(\hat{r}_2 sin(\omega\tau) - \hat{r}_3 cos(\omega\tau)\right)\right] \tag{7}$$

and

$$\approx \frac{1}{4\pi}\frac{\hat{r}_i}{|\vec{r}|c}\frac{\partial F_i}{\partial t} \tag{8}$$

if $y_0 \to 0$ and the effects of rotation are ignored. Eq. (8) is the result shown by Howe (2003) and Blake Vol. I (1986a). In the present work, as is done in Blake Vol. II (1986b), the individual blades are taken as the integration surface; this can be extended such that the blades are composed of k thin strips. This does not break the assumption that the acoustic surface is stationary. The compact point forces can be thought of as moving on an axisymmetric cylinder of radius y_0 that includes the space between the blades. The symmetry of the cylinder allows the locations of the point forces to move on the immobile surface. The k concentric cylinders are then superimposed to predict the acoustic field generated by the entire propeller. For the current work $k = 5$.

3 RESULTS

LES is performed at the design advance ratio $J = 0.889$ and a Reynolds number of $Re = 894,000$. The advance ratio J and Reynolds number Re are defined as:

$$J = \frac{U}{nD} \quad \text{and} \quad Re = \frac{UD}{\nu},$$

where U is the free-stream velocity, n is the propeller rotational speed and D is the diameter of the propeller disk. The notation used throughout the paper is as follows. Thrust, T, is the axial component of force and torque, Q, is the axial component of the moment of force. The non-dimensional thrust coefficient, K_T, and torque coefficient, K_Q, are given by:

$$K_T = \frac{T}{\rho n^2 D^4} \quad \text{and} \quad K_Q = \frac{Q}{\rho n^2 D^5},$$

where ρ is the density of the fluid. The readers are referred to Kumar and Mahesh (2017) for detailed validation of the simulations presented in this paper.

3.1 The propeller wake

The instantaneous axial velocity and pressure field of the propeller wake is shown in Figure 2. The near field is dominated by coherent tip vortices and the blade trailing edge wake. These vortical structures become unstable and eventually break up to form the far wake. The vortex cores are seen clearly in contours of pressure field as a region of low pressure. The region inside the hub vortex has the lowest pressure, and hence is more susceptible to cavitation. The hub vortex region remains coherent with minor oscillations in the far field.

The flow field is phase-averaged for more than 15 rotations after the transients die out. The phase-averaged axial velocity and vorticity magnitude are shown in Figure 3. The flow accelerates through the propeller, which is followed by slipstream contraction and eventual straining of the axial velocity field. Except near the axis (hub vortex region), the propeller wake has higher axial velocity than the freestream, which makes it different from other rotor wakes such as wind turbines. The vorticity field in Figure 3(b) shows distinct tip vortices and thin blade trailing edge wake in the near field. The tip vortices become more and more indistinguishable going downstream into the far wake.

3.2 Propeller loads

Unlike in off-design conditions, like crashback (Jang and Mahesh, 2013), the deviation of loads from the mean is small at design conditions. The contribution of pressure and viscous forces to the thrust generated by the propeller is shown in Figure 4(a). Note that the viscous force is negative. The magnitude of the viscous contribution to thrust is compared to that of pressure. The pressure force is two orders of magnitude higher than that of the viscous force generated by the propeller.

The frequency spectra of the loads are computed by dividing the time history into a finite number of segments with 50% overlap, applying a Hann window and rescaling to maintain the input signal energy. Each such segment is then transformed into the frequency domain by taking a Fast Fourier Transform (FFT). The power spectral density (PSD) is then averaged over all the segments. Figure 4(b) shows the PSD of the magnitude of K_T and K_Q as a function of non-dimensionalized frequency (rev^{-1}). The unsteady loads on the propeller are broadband at design loading as evident from the PSD of both K_T and K_Q.

3.3 Dynamic analysis of the propeller wake

The axial evolution of the propeller wake, along with the instability mechanisms and the flow field statistics, at design condition are thoroughly discussed in Kumar and Mahesh (2017). In this paper, we focus on the dynamics of the propeller wake. The velocity signals are acquired from LES at 30 probe points in the wake, 10 points each at: the axis (hub vortex), $70\%R$ from the axis (mid blade), and $90\%R$ from the axis (tip vortices), where R is the radius of the propeller. The locations of these probes are listed in Table 1. Felli et al. (2011) computed power spectra of the radial velocity at the edge of the wake and showed that the near field is dominated by the blade frequency followed by the shaft (rotor) frequency. As one moves downstream, the energy of the blade frequency is transferred to the shaft frequency following complex grouping mechanisms, which depend on the number of blades. They varied the number of blades from 2 to 4 and showed that for all cases, the far wake has a dominant shaft frequency followed by a power-law decay with an exponent of -0.9. A similar power-law exponent is also reported by Muscari et al. (2013) in the spectra of kinetic energy obtained from simulations using DES for the same rotor as Felli et al. (2011). In order to separate the effect of periodic forcing due to blade passage, they also report spectra of phase-averaged kinetic energy, which showed -0.9 power-law decay at higher frequencies as well.

Our simulations are performed in the rotating reference frame, hence the probes record phase-average velocity signals everywhere . The phase-averaging purges the effect of forcing due to periodicity and highlights all other effects. The frequency spectra of the phase-averaged radial velocity signals are computed in the same fashion as was described earlier for the force spectra. The frequency is normalized such that the shaft (rotor) frequency is $1rev^{-1}$.

The spectra of phase-averaged radial velocity, in the region of tip vortices, are shown in Figure 5. All the signals from T1-T10 show a dominant peak at $1rev^{-1}$, which is the shaft (rotor) frequency as expected. Distinct high frequecy peaks appear in the near field spectra (5a) around $100rev^{-1}$ along with higher harmonics. This seems to be related to the complex interactions between the tip vortices and the blade trailing edge wake. Once the tip votices become unstable and the blade trailing edge wake breaks up into smaller vortices after spiral roll-up (see Figure 2), these high frequencies are absent as seen in Figure 5(b). Also, the energy in the far wake is distributed across more frequencies when compared with the near wake.

Table 1: The coordinates of probes in the xy plane used to acquire velocity.

$y/D = 0$		$y/D = 0.35$		$y/D = 0.45$	
Probe	x/D	Probe	x/D	Probe	x/D
H1	0.5	M1	0.2	T1	0.2
H2	0.75	M2	0.4	T2	0.4
H3	1.0	M3	0.6	T3	0.6
H4	1.5	M4	0.8	T4	0.8
H5	2.0	M5	1.0	T5	1.0
H6	3.0	M6	1.5	T6	1.5
H7	4.0	M7	2.0	T7	2.0
H8	5.0	M8	3.0	T8	3.0
H9	6.0	M9	4.0	T9	4.0
H10	7.0	M10	5.0	T10	5.0

The spectra of phase-averaged radial velocity in the mid-blade region (Figure 6) show trends similar to those in the

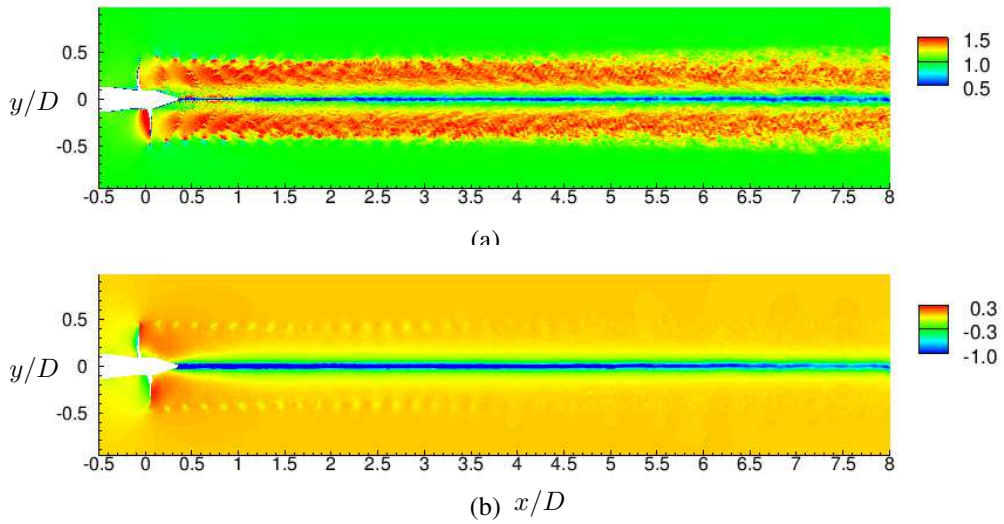

Figure 2: Instantaneous flow field in the xy plane: (a) axial velocity and (b) pressure. (Figures reproduced with permission from Kumar and Mahesh (2017)).

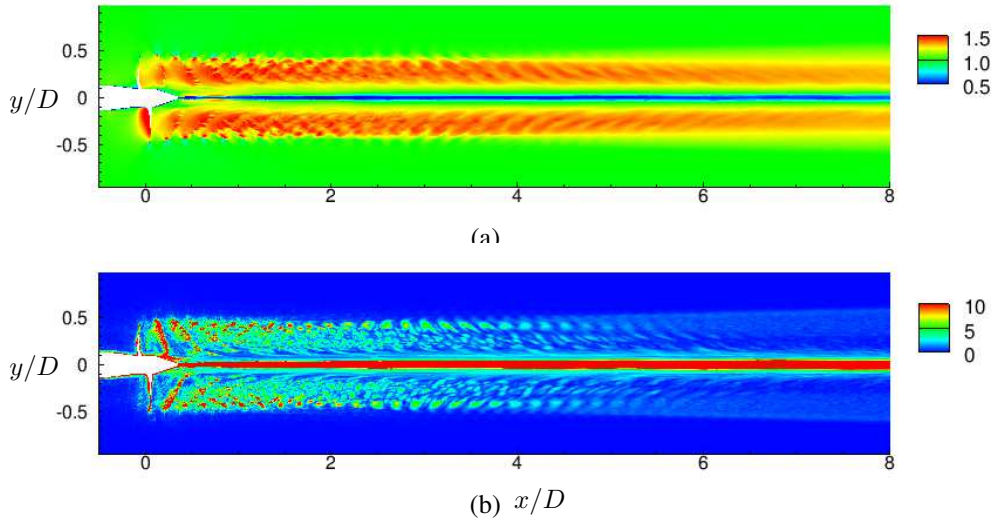

Figure 3: Phase-averaged flow field in the xy plane: (a) axial velocity and (b) vorticity magnitude. (Figures reproduced with permission from Kumar and Mahesh (2017)).

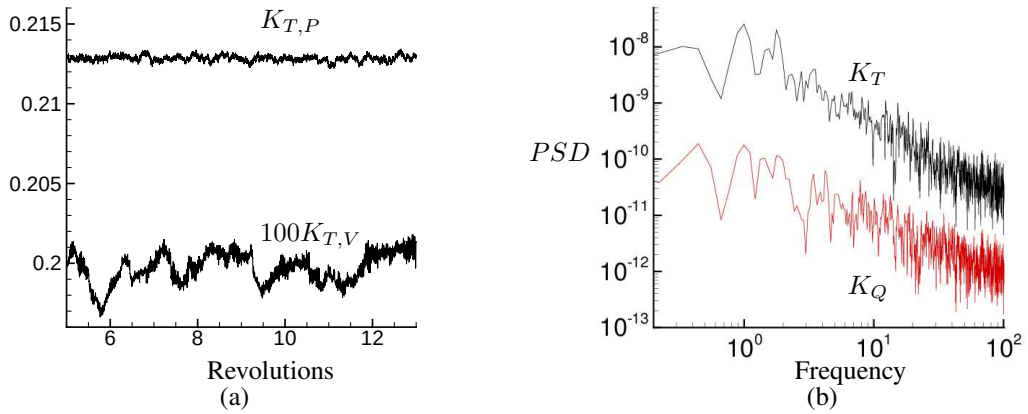

Figure 4: (a) Pressure and viscous contributions to thrust generated by the propeller and (b) PSD of unsteady loads, K_T and K_Q. (Figures reproduced with permission from Kumar and Mahesh (2017)).

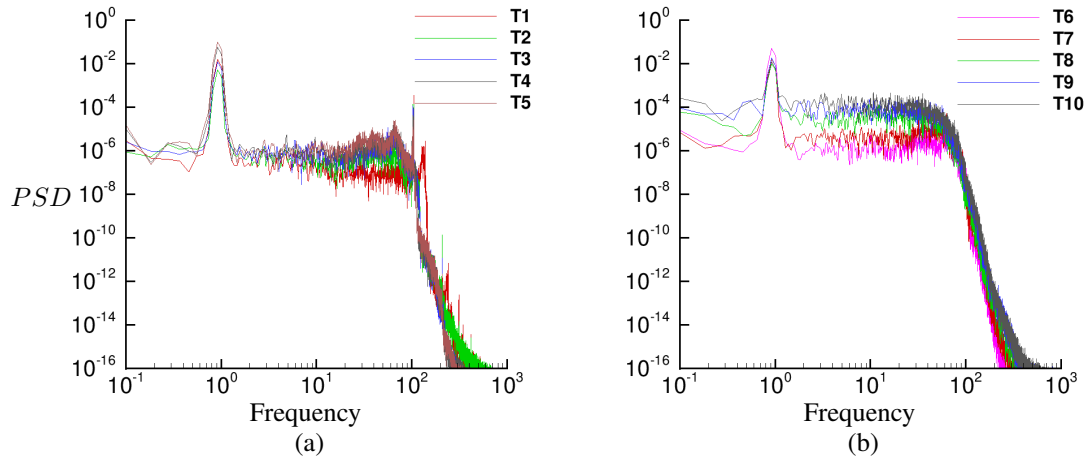

Figure 5: PSD of phase-averaged radial velocity at $90\%R$ from the propeller axis : (a) probes T1-T5 and (b) probes T6-T10. See Table 1 for coordinates.

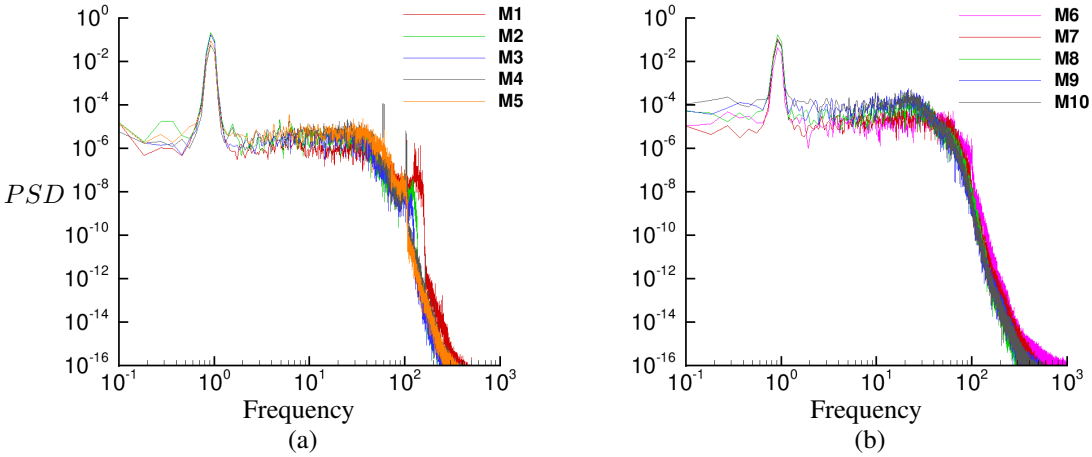

Figure 6: PSD of phase-averaged radial velocity at $70\%R$ from the propeller axis : (a) probes M1-M5 and (b) probes M6-M10. See Table 1 for coordinates.

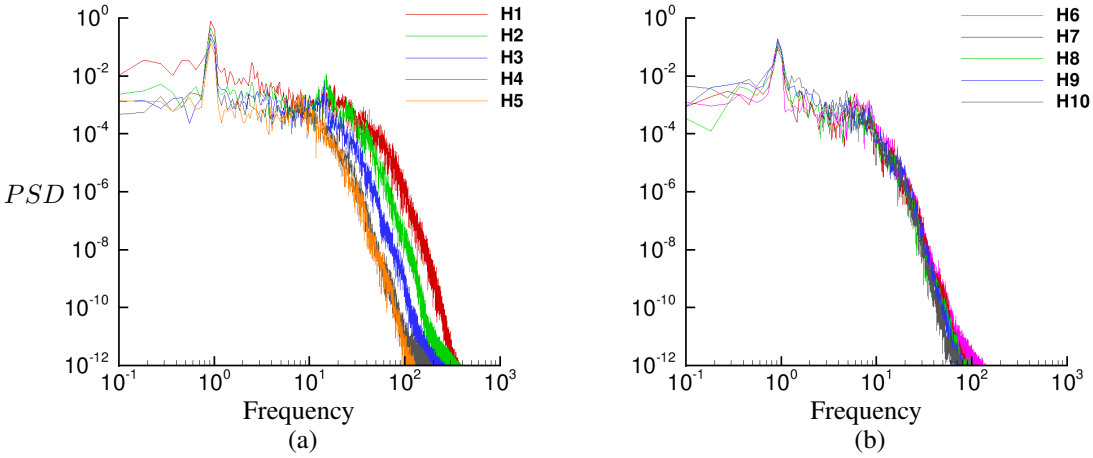

Figure 7: PSD of radial velocity on the propeller axis: (a) probes H1-H5 and (b) probes H6-H10. See Table 1 for coordinates.

tip vortex region. The major difference from the spectra of the tip vortex region is a better collapse of all spectra in the far wake. The radial velocity spectra in the hub vortex region is shown in Figure 7. In the near field (H1-H3), the spectra contained higher energy at the frequencies lower than the shaft frequency. This can be attributed to the geometrically induced flow separation on the hub (Figure 2a). The energy contained at high frequencies decreases moving downstream and eventually the spectra collapse as seen in Figure 7(b).

3.4 Propeller noise

Figure 8 shows directivity plots of sound pressure level (SPL) when the propeller is assumed compact and taken to be a net point force (with and without the hub) and when the propeller is not compact but the strips on individual blades are compact (with and without rotation). The angle $\theta = 0°$ is aligned with the direction of the wake and all sound was calculated at an observer radius of $100D$. Good agreement is seen across all the models. From this figure, it appears that the unsteadiness of the hub vorte contributes mostly to oscillations in the side force leadin to the the differences in SPL near $\theta = 90°/270°$. Thi implies that when predicting far field sound pressure level for this propulsor, operating at design conditions, the lov Mach number leads to the problem being very acoustically compact which allows the size of the propulsor and th rotation rate to be neglected while maintaining very goo agreement.

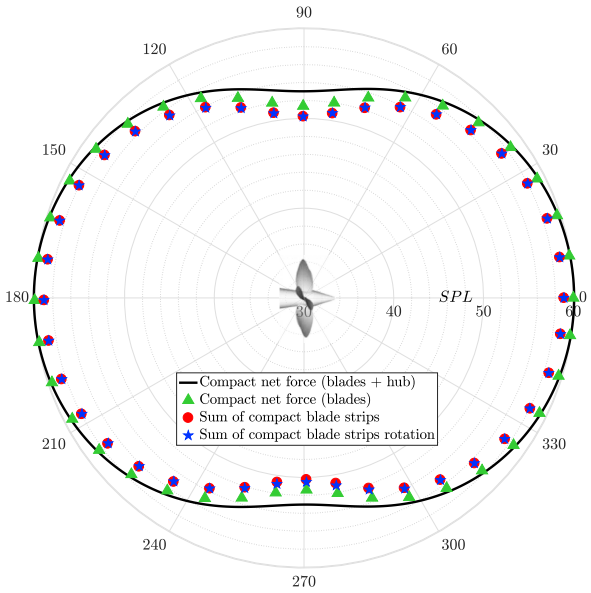

Figure 8: A directivity plot perpendicular to the rotor plane comparing sound pressure level (SPL) from each of the four acoustic models; every tenth data point has been plotted for clarity. The largest differences are visible in the rotational plane at $90°$ ($+\hat{y}$ axis) and $270°$ ($-\hat{y}$ axis) due to the unsteadiness of the hub. All of the models show good agreement.

Analysis of the sound generated by the independent radial strips on each blade, however, gives insight into some of the physics of noise production. Figure 9 shows that from the blade root to the point of maximum loading, the unsteadiness in side force is the main contributor to the sound produced by the blade at that location; near the tip the unsteadiness due to the presence of the tip vortex causes thrust to be the main contributor. This is highly localized around the tip, but the effects are large enough to result in each individual blade having a dipole directivity with the primary axis perpendicular to the dipole of the propeller as a whole, as shown in Figure 10. The acoustic compactness and equal blade spacing of this problem lead to the contributions from side force destructively interfering, while the sound generated by thrust from each blade interferes constructively. It should be pointed out that summing the side forces over all blades does not perfectly cancel the sound in the rotor plane; the large amplitude periodic changes in side force (which would produce strongly tonal noise) cancel when summed over all blades leaving small amplitude fluctuations when compared with the result of the constructive interference in thrust generated sound. The effects of the cancellation are apparent in Figure 11 where the directivities summed over all blades show alignment with the

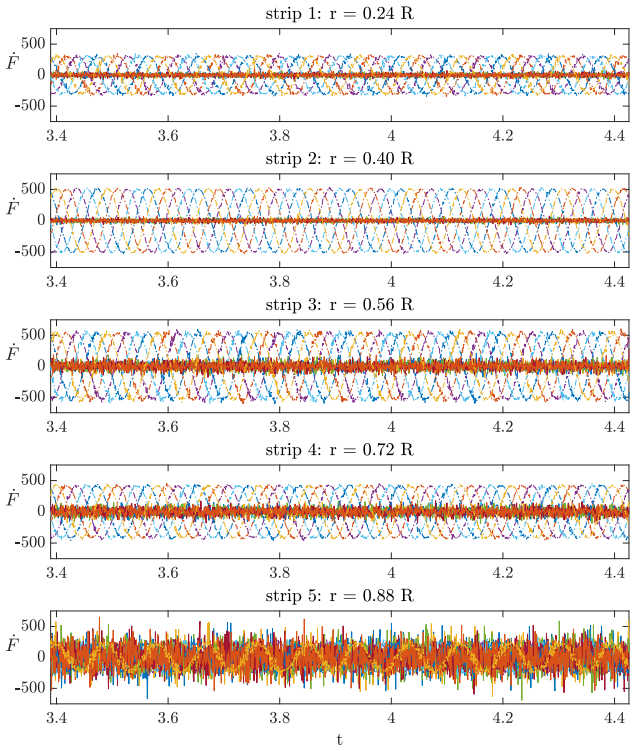

Figure 9: Time histories of $\partial F/\partial t$ at each radial location on the propeller. Thrust and the y component of the side force are plotted for all blades at each radial location. Blade 1: $\dot{T}$(—), $\dot{F}_y$(– ·), blade 2: $\dot{T}$(—), $\dot{F}_y$(– ·), blade 3: $\dot{T}$(—), $\dot{F}_y$(– ·), blade 4: $\dot{T}$(—), $\dot{F}_y$(– ·), blade 5: $\dot{T}$(—), $\dot{F}_y$(– ·).

Figure 12 shows the acoustic energy spectra for each of the prediction methods. Spectra were calculated as described in §3.2. The sound used to generate the spectra was calculated at an observer angle of $\theta = 45°$ to examine the properties of the contributions from both thrust and side force. Comparing spectra of the sound with the hub being both present and omitted points to the effect of the hub vortex

being noticeable at low frequency and in the rotor plane. Also, comparing the two topmost plots on the right, it can be seen that the presence of the hub has flattened the spectrum and distributed energy to much higher frequencies. Comparing spectra when rotation was accounted for shows that the slow rotation of this problem leads to very little change, using this method. The plots on the right all show that this propeller is producing very broadband sound. The low tip loading and slow rotation of this propeller lead to no distinct tones being produced.

4 SUMMARY

LES is shown to accurately capture the complex unsteady wake of a five-bladed marine propeller at design operating condition. The simulations are validated with experiments, showing good agreement for mean velocity profiles and mean loads (Kumar and Mahesh, 2017). LES results show that the propeller wake undergoes streamtube contraction, which is followed by the onset of instabilities. The roll-up of the blade trailing wake generates smaller vortices, which interact with the tip vortices, driving the wake instability.

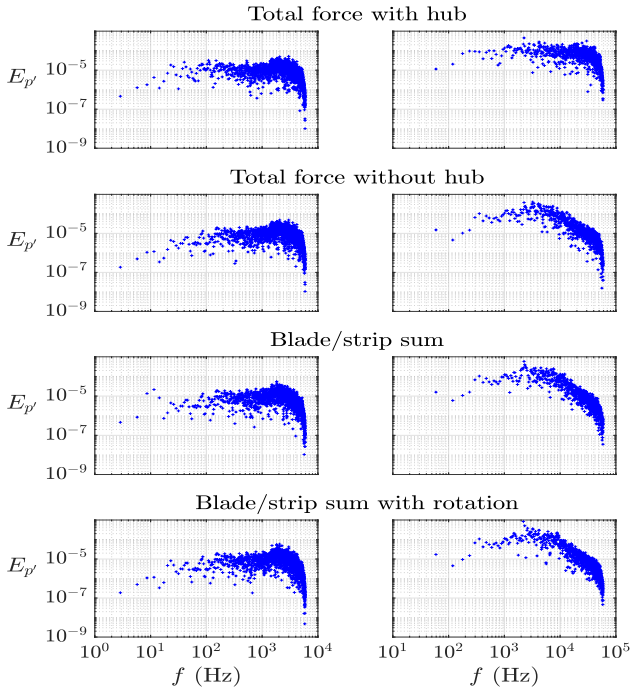

Figure 12: Acoustic energy spectra for each of the acoustic models at an angle of $\theta = 45°$. Plots on the left were calculated using a time history of 11.44 revolutions that resulted in a $f_{min} = 2.88$ Hz after windowing with 4 windows and 50% overlap. The Nyquist frequency was increased to investigate high frequencies as shown on the right plots with $f_{max} = 58.964$ kHz; the rotational frequency of the propeller is 11.03 Hz.

Once the propeller wake becomes unstable, the coherent vortical structures break up and evolve into the far wake composed of a fluid mass swirling around an oscillating hub vortex, which remains coherent over the entire length of the computational domain despite minor oscillations. The pressure forces contribute to almost all of the thrust produced by the propeller. The point spectra of radial velocity are computed at various streamwise locations in the tip vortex, mid blade, and hub vortex regions to analyze the spectral content of the propeller wake. The spectra collapse much better at all radial locations in the far wake than in the near wake.

Propeller blades are a dominant source of unwanted noise in submerged bodies. The computed flow field of the propeller wake in design condition is used to predict the far field noise using Curle's acoustic analogy modified for low-Mach flows. The computed unsteady loads form the strength of the dipole sources. The propeller produces a broadband noise at design condition. Although the tip portion of the blade has a small contribution to the loads, it is responsible for most of the unsteadiness and thus most of the noise produced by the rotor. The directivity plots of far field noise show that there is no appreciable change in the directivity even when the rotation effect is neglected. This is due to small rotation rate of the propeller at design condition.

ACKNOWLEDGEMENTS

This work is supported by the United States Office of Naval Research (ONR) under ONR Grant N00014-14-1-0289 with Dr. Ki-Han Kim as technical monitor. The computations were made possible through the computing resources provided by the U.S. Army Engineer Research and Development Center (ERDC) in Vicksburg, Mississippi on the Cray XE6, Copper and Garnet of High Performance Computing Modernization program (HPCMP). The authors also acknowledge the Minnesota Supercomputing Institute (MSI) at the University of Minnesota for providing resources that contributed to the research reported in this paper.

REFERENCES

Baek, D. G., Yoon, H. S., Jung, J. H., Kim, K. S., and Paik, B. G. "Effects of the advance ratio on the evolution of a propeller wake". Computers & Fluids, 118:32–43, 2015.

Balaras, E., Schroeder, S., and Posa, A. "Large-eddy simulations of submarine propellers". Journal of Ship Research, 59(4):227–237, 2015.

Blake, W. K. Mechanics of Flow-Induced Sound and Vibration. Volume I: General Concepts and Elementary Sources. Academic Press, Inc., 1986a.

Blake, W. K. Mechanics of Flow-Induced Sound and Vibration. Volume II: Complex Flow-Structure Interactions. Academic Press, Inc., 1986b.

Bridges, D. H. "A detailed study of the flowfield of a submarine propeller during a crashback maneuver". Technical Report MSSU-ASE-04-1, Department of Aerospace Engineering, Mississippi State University, 2004.

Chang, P., Ebert, M., Young, Y. L., Liu, Z., Mahesh, K., Jang, H., and Shearer, M. "Propeller forces and structural responses to crashback". In Proceedings of

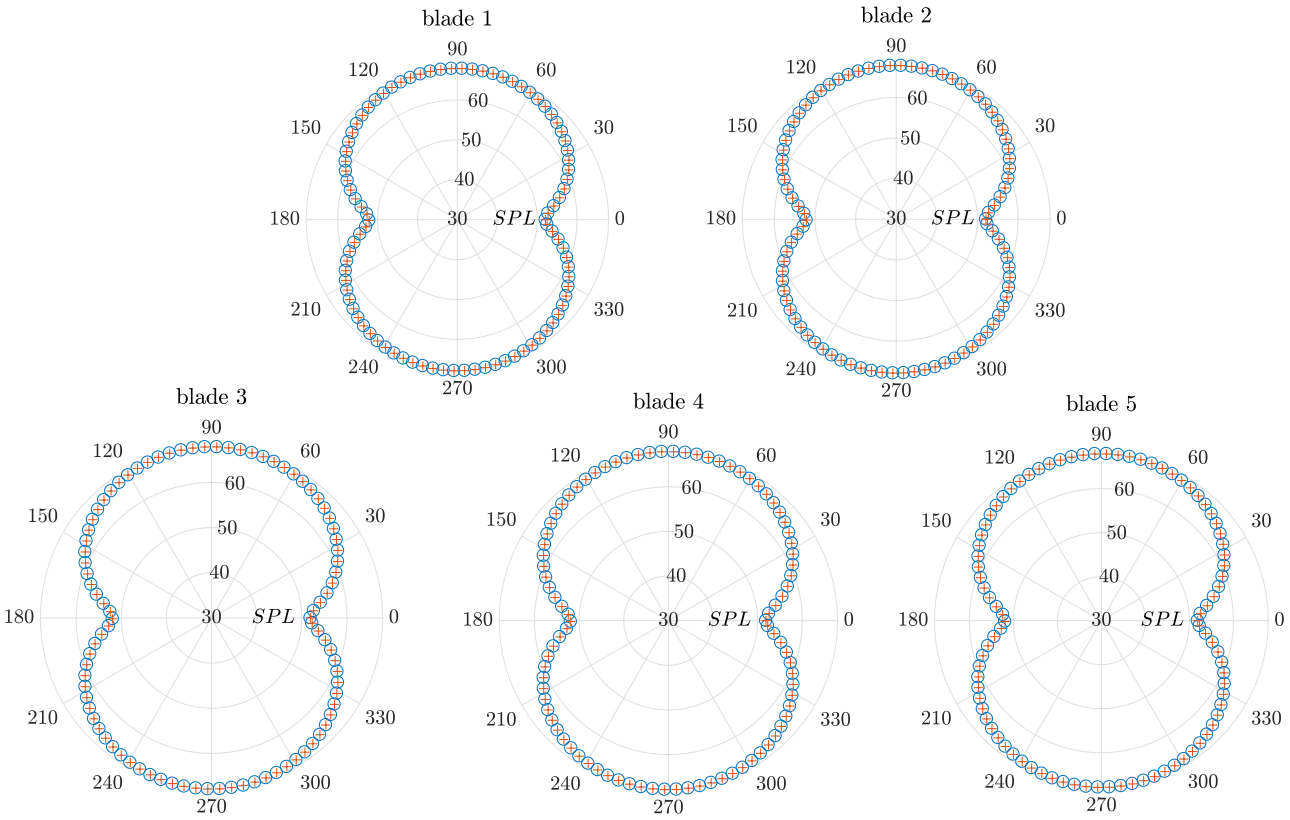

Figure 10: Directivities of sound pressure level for each blade of the propeller without rotation (○) and with rotation (+). Every 5th point is plotted for clarity.

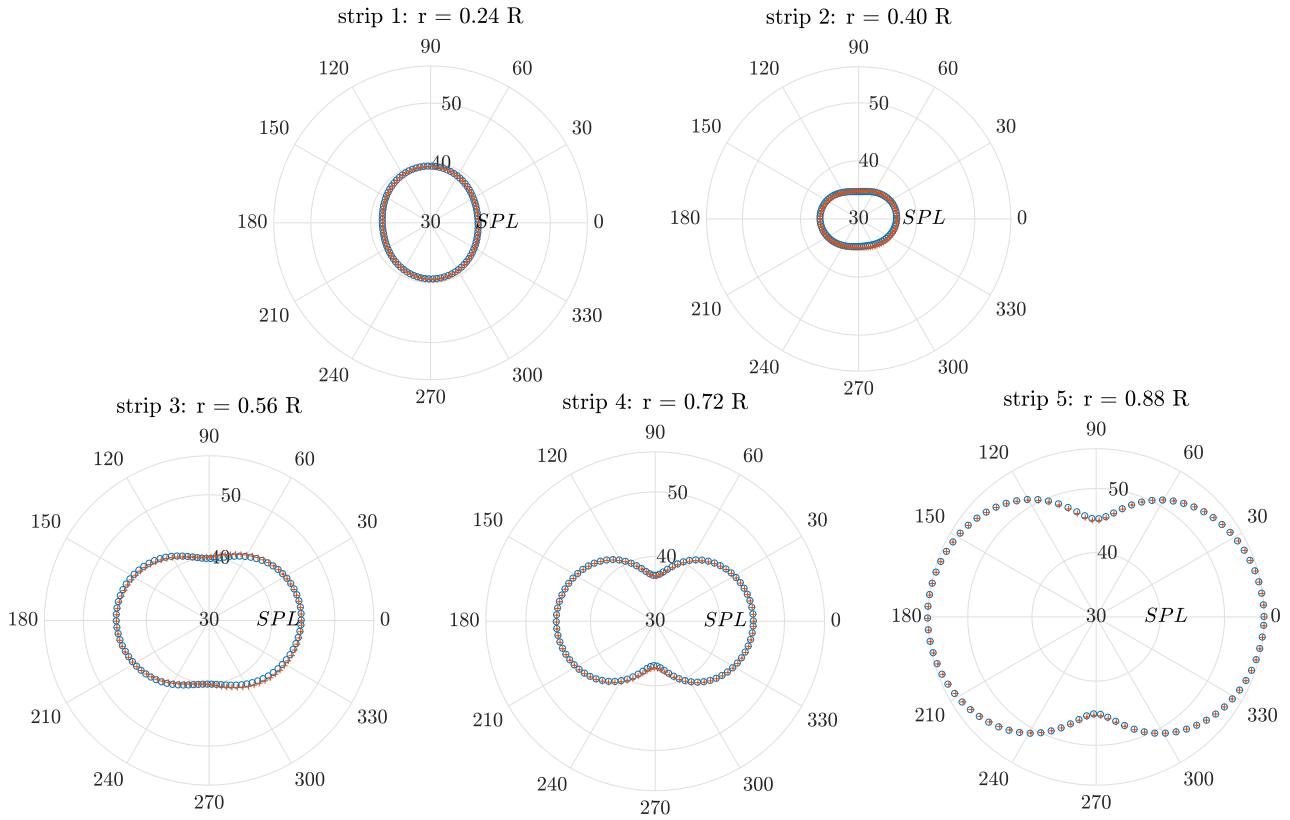

Figure 11: Directivities of sound pressure level for each radial strip summed over all blades without rotation (○) and with rotation (+). Every 5th point is plotted for clarity.

the 27th Symposium on Naval Hydrodynamics, Seoul, Korea, 2008.

Chang, P.A., Vargas, A., Lummer, D., Jiang, M., and Mahesh, K. "Fully-resolved les of weakly separated flows". In 20th AIAA Computational Fluid Dynamics Conference. AIAA, 2011.

Chase, N. and Carrica, P. M. "Submarine propeller computations and application to self-propulsion of DARPA Suboff". Ocean Engineering, 60:68–80, 2013.

Curle, N. "The influence of solid boundaries upon aerodynamic sound". Proceedings of the Royal Society of London, 231(1187):505–514, 1955.

Di Felice, F., Di Florio, D., Felli, M., and Romano, G. P. "Experimental investigation of the propeller wake at different loading conditions by particle image velocimetry". Journal of Ship Research, 48(2):168–190, 2004.

Di Felice, F., Felli, M., Liefvendahl, M., and Svennberg, U. "Numerical and experimental analysis of the wake behavior of a generic submarine propeller". In First International Symposium on Marine Propulsors, Trondheim, Norway, 2009.

Di Mascio, A., Muscari, R., and Dubbioso, G. "On the wake dynamics of a propeller operating in drift". Journal of Fluid Mechanics, 754:263–307, 2014.

Felli, M., Di Felice, F., Guj, G., and Camussi, R. "Analysis of the propeller wake evolution by pressure and velocity phase measurements". Experiments in Fluids, 41(3): 441–451, 2006.

Felli, M., Guj, G., and Camussi, R. "Effect of the number of blades on propeller wake evolution". Experiments in Fluids, 44(3):409–418, 2008.

Felli, M., Camussi, R., and Di Felice, F. "Mechanisms of evolution of the propeller wake in the transition and far fields". Journal of Fluid Mechanics, 682:5–53, 2011.

Ffowcs-Williams, J. E. and Hawkings, D. L. "Sound generation by turbulence and surfaces in arbitrary motion". Philosophical Transactions of the Royal Society of London, 264(1151):321–342, 1969.

Germano, M., Piomelli, U., Moin, P., and Cabot, W. H. "A dynamic subgrid–scale eddy viscosity model". Physics of Fluids A, 3:7:1760, 1991.

Gupta, B. P. and Loewy, R. G. "Theoretical analysis of the aerodynamic stability of multiple, interdigitated helical vortices". AIAA Journal, 12(10):1381–1387, 1974.

Howe, M. S. Theory of Vortex Sound. Cambridge University Press, 2003. ISBN 0521012236. doi: 10.1017/CBO9780511755491.

Jang, H. and Mahesh, K. "Large eddy simulation of ducted propulsors in crashback". In Proceedings of the 27th Symposium on Naval Hydrodynamics, 2008.

Jang, H. and Mahesh, K. "Large eddy simulation of crashback in ducted propulsors with stator blades". In Proceedings of the 29th Symposium on Naval Hydrodynamics, 2012.

Jang, H. and Mahesh, K. "Large eddy simulation of flow around a reverse rotating propeller". Journal of Fluid Mechanics, 729:151–179, 2013.

Joukowski, N. E. "Vortex theory of screw propeller". Trudy Otdeleniya Fizicheskikh Nauk Obshchestva Lubitelei Estestvoznaniya, 16(1):1–31, 1912. (in Russian).

Kerwin, J. E. "Marine propellers". Annual Review of Fluid Mechanics, 18(1):367–403, 1986.

Kumar, P. and Mahesh, K. "Analysis of marine propulsor in crashback using large eddy simulation". In Fourth International Symposium on Marine Propulsors, Austin, USA, 2015.

Kumar, P. and Mahesh, K. "Towards large eddy simulation of hull-attached propeller in crashback". In Proceedings of the 31st Symposium on Naval Hydrodynamics, Monterey, USA, 2016.

Kumar, P. and Mahesh, K. "Large eddy simulation of propeller wake instabilities". Journal of Fluid Mechanics, 814:361–396, 2017.

Lee, S. J., Paik, B. G., Yoon, J. H., and Lee, C. M. "Three-component velocity field measurements of propeller wake using a stereoscopic PIV technique". Experiments in Fluids, 36(4):575–585, 2004.

Levy, H. and Forsdyke, A. G. "The steady motion and stability of a helical vortex". Proceedings of the Royal Society of London. Series A, Containing Papers of a Mathematical and Physical Character, pages 670–690, 1928.

Lighthill, M. J. "On sound generated aerodynamically. i. general theory". In Proceedings of the Royal Society of London A: Mathematical, Physical and Engineering Sciences, volume 211, pages 564–587. The Royal Society, 1952.

Lilly, D. K. "A proposed modification of the Germano subgrid–scale closure model". Physics of Fluids A, 4:3: 633–635, 1992.

Mahesh, K., Constantinescu, G., and Moin, P. "A numerical method for large–eddy simulation in complex geometries". Journal of Computational Physics, 197:1: 215, 2004.

Muscari, R., Di Mascio, A., and Verzicco, R. "Modeling of vortex dynamics in the wake of a marine propeller". Computers & Fluids, 73:65–79, 2013.

Nemes, A., Lo Jacono, D., Blackburn, H. M., and Sheridan, J. "Mutual inductance of two helical vortices". Journal of Fluid Mechanics, 774:298–310, 2015.

Okulov, V. L. "On the stability of multiple helical vortices". Journal of Fluid Mechanics, 521:319–342, 2004.

Okulov, V. L. and Sørensen, J. N. "Stability of helical tip vortices in a rotor far wake". Journal of Fluid Mechanics, 576:1–25, 2007.

Park, N. and Mahesh, K. "Reduction of the Germano-identity error in the dynamic Smagorinsky model".

Physics of Fluids (1994-present), 21(6):065106, 2009.

Quaranta, H. U., Bolnot, H., and Leweke, T. "Long-wave instability of a helical vortex". Journal of Fluid Mechanics, 780:687–716, 2015.

Stella, A., Guj, G., Di Felice, F., and Elefante, M. "Propeller wake evolution analysis by LDV". In Proceedings of 22nd Symposium on Naval Hydrodynamics, Washington DC, pages 171–188, 1998.

Stella, A., Guj, G., and Di Felice, F. "Propeller wake flow-field analysis by means of LDV phase sampling techniques". Experiments in Fluids, 28(1):1–10, 2000.

Verma, A. and Mahesh, K. "A Lagrangian subgrid-scale model with dynamic estimation of Lagrangian time scale for large eddy simulation of complex flows". Physics of Fluids (1994-present), 24(8):085101, 2012.

Verma, A., Jang, H., and Mahesh, K. "The effect of an upstream hull on a propeller in reverse rotation". Journal of Fluid Mechanics, 704:61–88, 2012.

Vyšohlid, M. and Mahesh, K. "Large eddy simulation of crashback in marine propellers". In Proceedings of the 26th Symposium on Naval Hydrodynamics, Rome, Italy, 2006.

Widnall, S. E. "The stability of a helical vortex filament". Journal of Fluid Mechanics, 54(04):641–663, 1972.